



Aptamer-conjugated magnetic Fe₃O₄@Au core-shell multifunctional nanoprobe: A three-in-one aptasensor for selective capture, sensitive SERS detection and efficient near-infrared light triggered photothermal therapy of *Staphylococcus aureus*

Wenshi Zhao^{a,b,c}, Daxin Zhang^{a,b,c}, Tianxiang Zhou^c, Jie Huang^c, Yushan Wang^c, Boxun Li^d, Lei Chen^c, Jinghai Yang^{c,*}, Yang Liu^{c,*}

^a Changchun Institute of Optics, Fine Mechanics and Physics, Chinese Academy of Sciences, Changchun 130033, PR China

^b University of Chinese Academy of Sciences, Beijing 100049, PR China

^c Key Laboratory of Functional Materials Physics and Chemistry of the Ministry of Education, Jilin Normal University, Changchun 130103, PR China

^d Department of Chemistry, University of Jilin, No. 2699 Qianjin Street, Changchun, Jilin Province, 130012, PR China

ARTICLE INFO

Keywords:

Surface-enhanced Raman scattering (SERS)

Aptasensor

Fe₃O₄@Au-Apt NCs

Staphylococcus aureus (*S. aureus*)

Photothermal therapy (PTT)

ABSTRACT

Early and accurate diagnosis of pathogenic bacteria is essential to prevent further infection from spreading and multiplying. Herein, an aptamer (Apt) biosensor based on Fe₃O₄@Au nanocomposites (NCs) has been proposed for capture, surface-enhanced Raman scattering (SERS) detection, and photothermal therapy (PTT) of *S. aureus*. Fe₃O₄@Au NCs become SERS substrate and photothermal agent due to superior surface plasmon properties and photothermal ability, while the aptamer immobilized on surface of Fe₃O₄@Au NCs acts as a capture agent. The detection limit of optimized Fe₃O₄@Au-Apt aptasensor for *S. aureus* is 25 cfu/mL, and cell capture efficiency (CCE) is as high as 68%. Moreover, our Fe₃O₄@Au-Apt NCs have high photothermal conversion efficiency of 39.28%, which have been proven as an excellent photothermal agent. As verified by experiments, Fe₃O₄@Au-Apt aptasensor is not only a promising tool to detect and photothermally inactivated *S. aureus* in milk samples, but also exhibits negligible cytotoxicity and good biocompatibility. This work shows a promising multifunctional nano-platform, which has great potential in specific recognition, sensitive SERS detection and PTT of *S. aureus*.

1. Introduction

Staphylococcus aureus (*S. aureus*), a representative of Gram-positive bacteria, is a common foodborne pathogenic microorganism and is widely existed in the natural environment [1–3]. Research shows that *S. aureus* can cause various diseases, from skin infections to illnesses endangering human health, including meningitis, impetigos, conjunctivitis, parotitis and so on [4]. Over the past few years, there have been many reports of foodborne infections caused by the ingestion of enterotoxin produced by *S. aureus* [5]. More seriously, even low doses of pathogenic bacteria may spread to tissues or organs, and thus lead to excessive tissue damage [6,7]. Hence, it is of great significance to develop a quick, sensitive, and rapid efficient technique for *S. aureus* detection. Unfortunately, most studies have only focused on the construction of the single-function biological system for either detection or

killing of *S. aureus* so far [8]. Few studies have been devoted to combining selective detection and inactivation of *S. aureus* to avoid poisoning and infection of *S. aureus* and ensure food safety to the utmost extent.

To date, a considerable number of researches have been devoted to the accurate detection of *S. aureus* and methods mainly include bacterial culture method, ELISA, ICS and PCR [9]. Although these methods have their own advantages, they have their respective limitations. For example, bacterial culture procedure has the advantages of simple operation, relatively low-cost, and it can be applied to quantitatively detect *S. aureus*. However, it is complicated and time-consuming, which is not suitable for the emergency events of public health [10,11]. Immunological method can achieve the real-time detection of *S. aureus* conveniently and provide test results in a short time, but it cannot obtain the expected forecasting accuracy due to low sensitivity [12]. By

* Corresponding authors.

E-mail addresses: jhyang1@jlnu.edu.cn (J. Yang), liuyang@jlnu.edu.cn (Y. Liu).

<https://doi.org/10.1016/j.snb.2021.130879>

Received 15 June 2021; Received in revised form 21 August 2021; Accepted 4 October 2021

Available online 7 October 2021

0925-4005/© 2021 Elsevier B.V. All rights reserved.

comparison, although PCR is a highly sensitive and easy to operate technique, PCR-based technique needs tedious sample pre-treatment steps and qualified and trained laboratory personnel [13].

Recently, surface-enhanced Raman scattering (SERS) is regarded as a promising method for pathogen bacterial identification and detection because of various advantages of simple operation, on-site convenience, time-saving, super-sensitivity and non-destructiveness [14–16]. SERS can enhance Raman scattering signal intensity by molecules adsorbed on rough metal surfaces [17]. It is widely believed that the two enhancement mechanisms of SERS are electromagnetic enhancement (EM) and chemical enhancement (CE) [18]. The enhancement of the former mainly comes from the localized surface plasmon resonance (LSPR) of noble metal nanostructures, which is widely regarded as the dominant factor for SERS, while the latter is derived from the charge transfer (CT) between the adsorbates and substrates [19]. In general, SERS-based detection of bacteria mainly consists of two approaches [20]. One is to detect bacteria indirectly by achieving the SERS signals of reporter molecules adsorbed on the surfaces of bacteria. For instance, Zhang et al. designed a SERS biosensor with sandwich structure and realized the quantitative detection of *S. aureus* indirectly [21]. Zhang et al. proposed and constructed a dual-recognition SERS biosensor, and DTNB and 4-MBA were chosen as Raman reporter molecules to simultaneously detect two pathogens [22]. Despite high sensitivity and low detection limit, an indirect SERS detection of bacteria method only provides fingerprint vibrational information of Raman reporter molecules instead of the target bacteria, which is hard to accomplish the goal of high selectivity in bacteria distinction. By contrast, the other label-free SERS approach can obtain the inherent SERS fingerprint of bacteria and can discriminate different bacteria from biological matrix [23]. For instance, Chen and co-workers presented a SERS method that uses Ag nanoparticles (NPs) with positive charge to directly discern methicillin-resistant *S. aureus* [24].

There is no denying that the design and construction of a highly sensitive and recyclable SERS substrate is essential to obtain high SERS performance and promote the practical application of SERS biosensors. The noble metals, such as Ag and Au, are commonly used SERS substrates because of their characteristic plasmonic properties [25]. However, Ag substrates are easily oxidized and the bactericidal properties of Ag NPs can result in undesirable effects such as DNA denaturation, which are adverse to applications of SERS for detection in biological and biomedical fields [26]. Contrary to Ag NPs, the Au-based SERS substrates exhibit high stability and biocompatibility, which determine that Au NPs are more promising SERS-active substrates. More importantly, Au NPs can serve as near-infrared (NIR) hyperthermia agents in photothermal therapy (PTT) due to LSPR characteristic and facile surface functionalization [27–29]. PTT is a novel noninvasive therapeutic method by converting NIR laser energy into heat, which can induce a local temperature increase and thus reaching the goal of eradicating targeted cancer cells or bacteria [30–32]. The combination of PTT with SERS technology is extremely important to build novel theranostic platforms with precise localization and monitor of therapeutic response [33]. Although Au NPs show a high photothermal conversion efficiency, the high price of Au NPs has seriously hampered the promotion and applications of PTT. The combination of magnetic oxides, especially superparamagnetic Fe₃O₄ NPs, and noble metals in core-shell nanocomposites (NCs) has been proved to be a valid way to overcome shortcomings [34]. Interestingly, the existence of superparamagnetic Fe₃O₄ NPs not only can make Au NPs recyclable, but also can aggregate readily the target bacteria from complex systems by an external magnetic field to reduce testing time [22,35,36]. For example, 3D Fe₃O₄@Au NCs were assembled successfully and used for photothermal ablation and SERS detection of microorganisms [37].

Selective recognition ability is another important index to evaluate the performance of SERS aptasensor. Antibodies are the most commonly bio-recognition molecules due to high sensitivity and specificity, but high production cost and poor stability severely restrict their

widespread applications [38]. Aptamers (Apt) are artificial single-stranded (DNA or RNA) oligonucleotide sequences chemically synthesized in vitro, which have considerable advantages over antibodies as recognition elements [17,39,40]. On one hand, aptamers can be produced by simple, fast and economic preparation way and can rival conventional antibodies in sensitivity [41]. On the other hand, aptamers are more stable than antibodies and are less affected by issues such as temperature and pH value. Additionally, aptamers with high specificity can be flexibly modified with various functional groups with high affinity to bind to the target [42]. Extensive research has been devoted to recognizing pathogenic bacteria by SERS substrates conjugated with aptamers and aptamers are considered as innovative alternatives to antibodies for selective recognition of bacteria [43]. However, according to our understanding, there are no reports on the utilization of Fe₃O₄@Au-Apt NCs for selective detection and killing of *S. aureus*.

Herein, we proposed and prepared a novel Apt-conjugated Fe₃O₄@Au nanoprobe that realized the integration of selective capture, sensitive SERS detection and NIR-mediated PTT of *S. aureus* in complex matrices. Multifunctional aptasensor consisted of magnetic Fe₃O₄ core and Au shell, and then was functionalized with aptamer as specific recognition moiety for target *S. aureus*. By recording SERS signal intensities of 4-MBA at different concentrations, the SERS enhancement mechanism of Fe₃O₄@Au NCs was discussed. After modification with aptamer, the ability of Fe₃O₄@Au-Apt aptasensor to capture and enrich *S. aureus* from the solution was studied. After optimizing the experimental parameters including the concentration of aptamer, the incubation time between the aptamer and Fe₃O₄@Au NCs and the incubation time between the *S. aureus* and Fe₃O₄@Au-Apt aptasensor, the successfully obtained Fe₃O₄@Au-Apt NCs could be applied to achieve rapid, ultra-sensitive and specific SERS detection and photothermal inactivation of *S. aureus* under NIR light irradiation. Additionally, Fe₃O₄@Au-Apt NCs could realize the integration of SERS detection and killing of *S. aureus* in milk samples. Our work not only further reveals the SERS enhancement and photothermal conversion mechanism of Fe₃O₄@Au-Apt NCs, but also presents a wide variety of possibilities for applications in selective detection and inactivation of bacteria in complex matrices.

2. Materials and methods

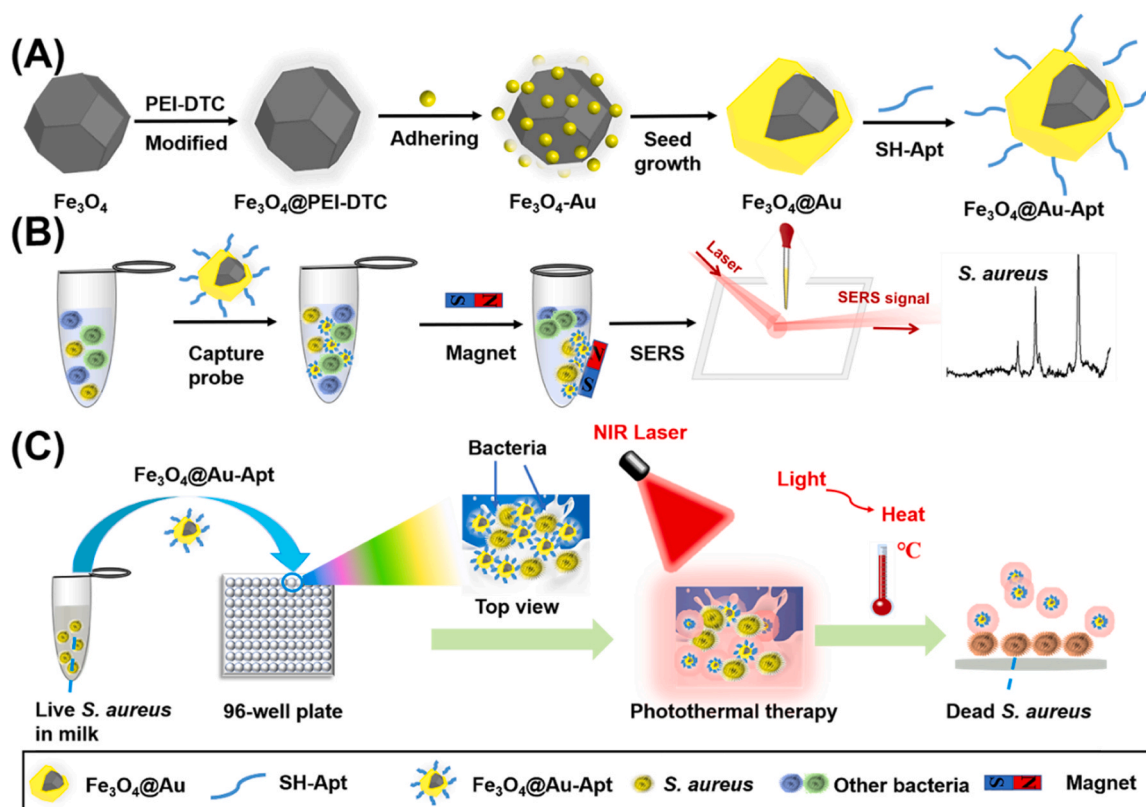
The chemicals, biochemicals and instruments are presented in the [Supporting Information](#).

2.1. Preparation of Fe₃O₄@Au-Apt NCs

The preparation procedures of Au NPs, Fe₃O₄ NPs and Au immobilized on PEI-DTC modified Fe₃O₄ (Fe₃O₄@Au NCs) were described in the [Supporting Information](#). Fe₃O₄@Au-Apt NCs were fabricated as follows, as present in [Scheme 1](#) (A). The thiolated aptamer (SH-Apt) needed to be activated by TCEP solution. Specifically, 10 μ L of SH-Apt with different concentrations (10^{-3} – 10^{-8} M) was mixed with 1 mM TCEP solution. After 1 h, the activated SH-Apt was mixed with 1 mg of Fe₃O₄@Au NCs and the mixture was incubated at 37 °C with gentle shaking by thermostatic oscillator for different times (8, 16, 24, 32, 40 and 48 h). After that, the mixture was soaked in 100 mM NaCl solution for 48 h. Finally, products were washed with PBS buffer under manual shaking.

2.2. SH-Apt modified Fe₃O₄@Au NCs for SERS detection of *S. aureus*

The preparation of *S. aureus* samples was shown in the [Supporting Information](#). *S. aureus* with concentration of 10^7 cfu/mL was incubated with SERS aptasensor for different time (5, 25 and 45 min) at temperature of 37 °C with shaking by thermostatic oscillator for *S. aureus* detection. After magnetic separation, Fe₃O₄@Au-Apt-*S. aureus* complex was washed at least five times and resuspended in 5 μ L of PBS buffer. Finally, products were dropped onto a glass slide for SERS detection.



Scheme 1. (A) Synthetic route for $\text{Fe}_3\text{O}_4@Au-Apt$ NCs and schematic diagram of (B) SERS detection and (C) NIR-triggered PTT for *S. aureus*.

Subsequently, *S. aureus* with different concentrations (10^2 - 10^7 cfu/mL) was incubated with SERS aptasensor for 25 min. The same procedure was carried out for *S. aureus* SERS detection.

2.3. Specificity analysis of SERS aptasensor and real sample analysis

For evaluating the specificity of the prepared SERS aptasensor, other samples including *Escherichia coli*, *Bacillus cereus*, *Vibrio parahaemolyticus*, *Salmonella typhimurium* and *Shigella dysenteriae* were selected as interferences in this experiment. Bacterial concentration was set to 10^7 cfu/mL for SERS detection. In general, after the milk in supermarket is treated at ultra-high temperature (UHT) or industrial sterilization, *S. aureus* with low heat-resistance in the milk can be inactivated. However, the breakage of packages during the transportation can lead to the contamination of milk and cause the breeding of bacteria. Milk purchased from Tmall supermarket was chosen as the actual sample for *S. aureus* detection.

2.4. Photothermal conversion performance of SH-Apt modified $\text{Fe}_3\text{O}_4@Au$ NCs

SH-Apt modified $\text{Fe}_3\text{O}_4@Au$ NCs with different concentrations (50, 150, 200, 300 $\mu\text{g}/\text{mL}$) were placed in the 96-well plates and irradiated with 808 nm laser (1.5 W cm^{-2} , facula 10 mm) for 5 min, and then cooled naturally. The temperature of water irradiated by 808 nm laser was measured as control. The solution temperature was recorded every 30 s by using an infrared thermal imaging camera.

2.5. NIR PTT of *S. aureus* in milk samples

For evaluating the photothermal effect of synthesized $\text{Fe}_3\text{O}_4@Au-Apt$ NCs in practical application, $\text{Fe}_3\text{O}_4@Au-Apt$ NCs were used to inactivate bacteria in milk samples. 20 μg of SH-Apt modified $\text{Fe}_3\text{O}_4@Au$ NCs was added to 150 μL of milk samples spiked with

S. aureus (10^3 cfu/mL). After being incubated for 25 min and irradiated by 808 nm laser for 5 min, photothermal effect of $\text{Fe}_3\text{O}_4@Au-Apt$ NCs for killing *S. aureus* was studied by the Calcein-AM/PI double staining kit, in which live bacteria emitted the green fluorescence and dead bacteria appeared red fluorescence based on the principle of dye exclusion [44]. All the fluorescence images were obtained using MicroSpec System. Furthermore, 150 μL of the complex solution was evenly spread on the LB agar plate and incubated at 37°C for 24 h. The number of colonies on LB agar plate was convenient for direct observation of surviving bacteria. Three sets of parallel experiments, including *S. aureus* in milk samples with or without laser treatment and *S. aureus* in milk samples incubated with $\text{Fe}_3\text{O}_4@Au-Apt$ NCs treatment only, were performed as control groups.

3. Results and discussion

3.1. Operating Principle of SERS aptasensor for the detection of *S. aureus* based on $\text{Fe}_3\text{O}_4@Au-Apt$ NCs

Scheme 1(B) shows the operating principle of $\text{Fe}_3\text{O}_4@Au$ NCs immobilized with aptamer for direct SERS detection of *S. aureus*. Firstly, SH-Apt was modified on surfaces of $\text{Fe}_3\text{O}_4@Au$ NCs through Au-S bond and then $\text{Fe}_3\text{O}_4@Au-Apt$ NCs were added to solutions with multiple bacteria to identify *S. aureus*. *S. aureus* could be selectively captured by $\text{Fe}_3\text{O}_4@Au-Apt$ NCs owing to the specific recognition of aptamer. Secondly, $\text{Fe}_3\text{O}_4@Au-Apt-S. aureus$ complex was separated with a magnetic field. After being rinsed with PBS buffer, $\text{Fe}_3\text{O}_4@Au-Apt-S. aureus$ complex was dropped on the glass slide for SERS detection of *S. aureus*. Finally, the target *S. aureus* in the sample can be quantified by the proportional relationship between logarithm of bacteria concentration and SERS intensity.

3.2. Structure and magnetic properties of $\text{Fe}_3\text{O}_4@Au$ NCs

Morphology of Fe_3O_4 NPs, Fe_3O_4 -Au NCs and $\text{Fe}_3\text{O}_4@Au$ NCs was tested by SEM, as shown in Fig. 1(A). Fig. 1A (a) shows that Fe_3O_4 NPs with a narrow size distribution are truncated octahedral in shape and the average size is about 70 nm. Au NPs with a diameter of 6 nm are distributed randomly onto the surfaces of Fe_3O_4 NPs, as presented in Fig. 1A (b). Due to the further reduction of Au^{3+} ions around nucleation sites, Au shell is formed on surfaces of Fe_3O_4 NPs and the average crystallite size increases to 80 nm (Fig. 1A (c)). EDS spectra in Fig. S1 shows that $\text{Fe}_3\text{O}_4@Au$ NCs consist of O, Fe and Au elements and SEM-EDS elemental mapping analysis in the inset of Fig. 1A (c) confirms Au NPs are evenly distributed on surfaces of Fe_3O_4 NPs. Additionally, XRD patterns in Fig. 1(B) shows typical diffraction peaks of Fe_3O_4 at 2θ values of 30.1, 35.4, 43.0, 53.4, 56.9, and 62.5° are ascribed to (220), (311), (400), (422), (511) and (440) crystalline planes of Fe_3O_4 (JCPDS 19-0629) [45]. After Au shell is grown over the surfaces of Fe_3O_4 NPs, four new XRD peaks are observed at $2\theta = 38.2, 44.4, 64.5$ and 77.5° , corresponding to diffractions from (111), (200), (220), and (311) of Au (JCPDS 04-0784) [46]. It can be found that the diffraction peak intensity of Fe_3O_4 is significantly reduced and almost disappears, which indicates indirectly the formation of Au shell on surfaces of Fe_3O_4 NPs. Optical properties of Fe_3O_4 NPs, Au NPs and $\text{Fe}_3\text{O}_4@Au$ NCs were studied by UV-Vis spectra presented in Fig. 1(C). As for Fe_3O_4 NPs, it can be observed that a broad spectrum spans a wide wavelength range, which can be attributed to the appearance of the black powder [47]. Au NPs show a characteristic LSPR peak centered at 520 nm, and full width at half maximum of ~ 59 nm indicates Au NPs have narrow size distribution. Compared with Au NPs, LSPR peak of $\text{Fe}_3\text{O}_4@Au$ NCs presents a significant red shift from 520 to 610 nm due to the altered dielectric environment of the plasmonic nanosurface, which indicates the formation of the Au shell on surfaces of Fe_3O_4 NPs [48]. In addition, the small shoulder at 400 nm is probably due to the uncapped Fe_3O_4 NPs [49]. Fig. 1(D) records the hysteresis loops of Fe_3O_4 NPs and $\text{Fe}_3\text{O}_4@Au$ NCs, and the saturation magnetization (M_s) is 68 and 46 $\text{emu}\cdot\text{g}^{-1}$,

respectively. Although the diamagnetism of Au shell reduces the M_s value, $\text{Fe}_3\text{O}_4@Au$ NCs remain have good magnetic response and can be quickly separated by a magnet. Furthermore, $\text{Fe}_3\text{O}_4@Au$ NCs are saturated at a low magnetic field, and the M-H loop is almost flat above the saturated magnetic field, manifesting that they are suitable for potential applications in the biomedical field.

3.3. SERS activity and mechanism of $\text{Fe}_3\text{O}_4@Au$ NCs

4-MBA, a probe molecule with stable and strong SERS signals, was used to investigate the SERS effect of $\text{Fe}_3\text{O}_4@Au$ NCs [50]. Detailed detection procedure is as follows. $\text{Fe}_3\text{O}_4@Au$ NCs were mixed with 4-MBA with different concentrations (10^{-3} to 10^{-9} M) for 3 h to allow the 4-MBA molecules to adhere to the surfaces. Then, $\text{Fe}_3\text{O}_4@Au$ NCs were collected with the help of a magnet and used for the SERS detection. The characteristic peak of 4-MBA at 1588 cm^{-1} was chosen to determine the linear relationship between concentration and SERS intensity, as shown in Fig. S2(A). The error bars in the inset of Fig. S2(B) represent the standard deviation from five independent SERS measurements. It can be seen that the 4-MBA solution with the concentration of 10^{-9} M still has a significant SERS signal, which is even better than results of other previous reports [51–53]. The high SERS performance of $\text{Fe}_3\text{O}_4@Au$ NCs may be attributed to the following combination of factors. Firstly, the choice of laser excitation wavelength is an important parameter for achieving high SERS sensitivity. In our experiment, 633 nm laser line was used to excited $\text{Fe}_3\text{O}_4@Au$ NCs, which is close to LSPR peak of $\text{Fe}_3\text{O}_4@Au$ NCs and thus leads to the enhancement of LSPR effect. Secondly, surface roughness can boost the density of SERS hot spot of SERS-active substrates. The relatively high roughness on the surfaces of $\text{Fe}_3\text{O}_4@Au$ NCs can be observed from SEM image resulting in the amplification of SERS intensity of 4-MBA on $\text{Fe}_3\text{O}_4@Au$ NCs [54]. Thirdly, because $\text{Fe}_3\text{O}_4@Au$ NCs are superparamagnetic, they are easily aggregated under external magnetic field and are likely to give rise to the formation of “sandwich” effect. In the “sandwich” effect, a probe molecule can be trapped by two or more adjacent SERS substrate NPs,

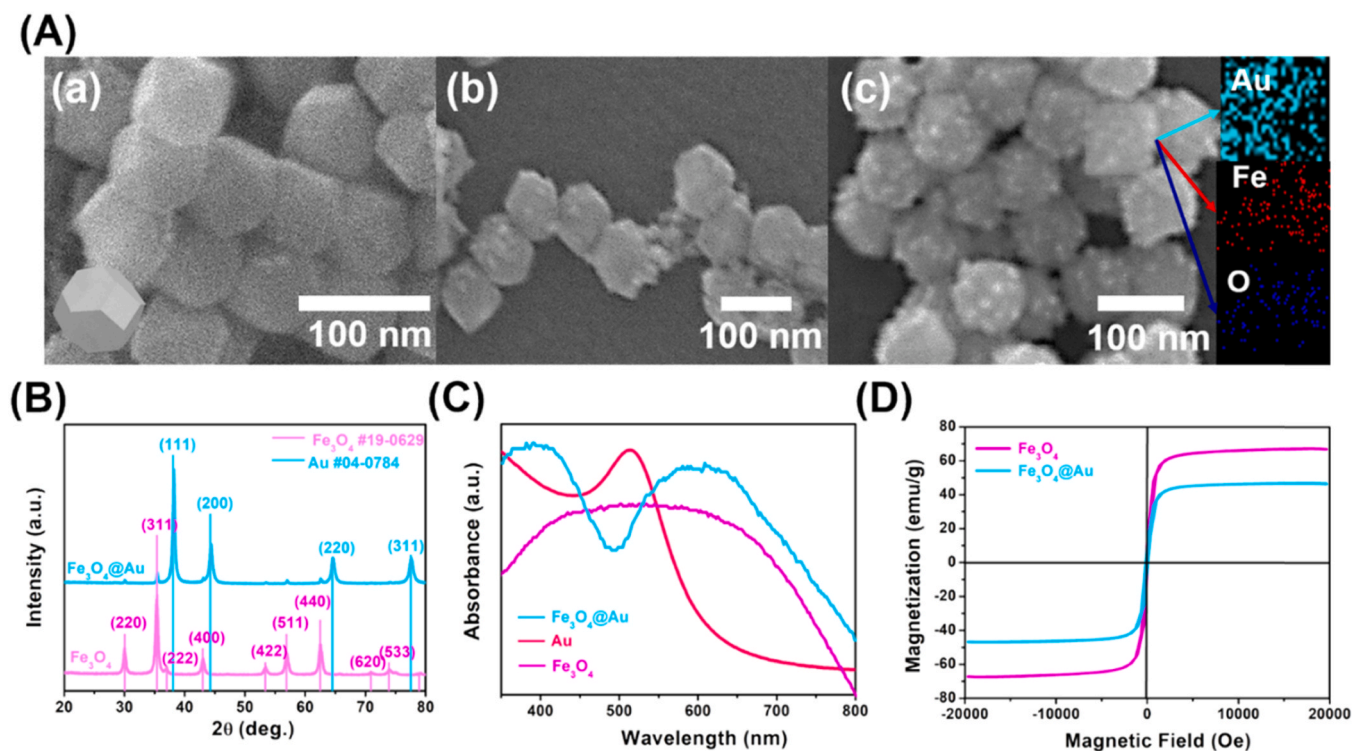


Fig. 1. (A) SEM images of (a) Fe_3O_4 NPs, (b) Fe_3O_4 -Au NCs, (c) SEM images and EDS elemental mapping images of $\text{Fe}_3\text{O}_4@Au$ NCs, (B) XRD patterns, (C) UV-Vis spectrum, (D) Magnetic hysteresis curves of Fe_3O_4 NPs and $\text{Fe}_3\text{O}_4@Au$ NCs.

which may contribute to the increase of SERS signals [49]. In addition, it can also be found that $\text{Fe}_3\text{O}_4\text{@Au}$ NCs show the stronger SERS enhancement effect than Au NPs, as shown in Fig. S2(C). Au NPs are prone to agglomerate because of the high surface area, which inevitably decreases the number of hot spots [55,56]. Immobilization of Au NPs on surfaces of Fe_3O_4 NPs can effectively inhibit the aggregation of Au NPs. Therefore, it is reasonable that $\text{Fe}_3\text{O}_4\text{@Au}$ NCs exhibit enhanced SERS signals of 4-MBA compared with Au NPs.

3.4. Characterization of surface properties of $\text{Fe}_3\text{O}_4\text{@Au-Apt}$ NCs

In order to establish a detection platform that can specifically identify the target, $\text{Fe}_3\text{O}_4\text{@Au-Apt}$ NCs were prepared by modifying the surfaces of $\text{Fe}_3\text{O}_4\text{@Au}$ NCs with aptamer. Zeta potentials of Fe_3O_4 NPs, Au NPs, $\text{Fe}_3\text{O}_4\text{@Au}$ NCs and $\text{Fe}_3\text{O}_4\text{@Au-Apt}$ NCs were measured, as presented in Fig. 2(A). Results indicate that Au NPs can be firmly adsorbed on the surfaces of PEI-DTC-modified Fe_3O_4 NCs, as demonstrated by the change of zeta potential value from +25.8 eV of Fe_3O_4 NPs to -23.9 eV of $\text{Fe}_3\text{O}_4\text{@Au}$ NCs [57]. After $\text{Fe}_3\text{O}_4\text{@Au}$ NCs are further functionalized with negatively charged aptamer through Au-S covalent bond, and zeta potential value of $\text{Fe}_3\text{O}_4\text{@Au-Apt}$ NCs further reduces to -32.2 eV, which confirms the formation of $\text{Fe}_3\text{O}_4\text{@Au-Apt}$ NCs [58]. The surface charge changes during the process can verify the formation of NCs. FTIR and UV-Vis absorption spectroscopy were also performed the successful modification $\text{Fe}_3\text{O}_4\text{@Au}$ NCs with aptamer. As seen in Fig. 2(B), after reacting with aptamer, new peaks appear. Peaks located at 1090 cm^{-1} and 1236 cm^{-1} are attributed to the symmetric and antisymmetric stretching vibrations of $-\text{PO}_2$ groups of aptamer, while the peak at 2850 cm^{-1} can be ascribed to $-\text{CH}_2$ groups in aptamer [59,60]. UV-Vis absorption spectroscopy in Fig. 2(C) shows that a typical absorption peak of aptamer at 260 nm is observed after modifying aptamer on the surfaces of which can be designated to $\text{C}=\text{C}=\text{C}$ conjugated double bond of purine and pyrimidine base [61]. At the same time, the absorption spectra of aptamer solution before and after

combining with $\text{Fe}_3\text{O}_4\text{@Au}$ NCs are shown in Fig. S3. After aptamer was conjugated to $\text{Fe}_3\text{O}_4\text{@Au}$ NCs, the supernatant solution was collected by centrifugation and then tested. The results show that compared with the solution before reaction, the intensity of absorption band at 260 nm is markedly decreased. Therefore, all these phenomena indicate that the aptamer is immobilized on the surfaces of $\text{Fe}_3\text{O}_4\text{@Au}$ NCs successfully. Fig. 2(D) shows the photograph of $\text{Fe}_3\text{O}_4\text{@Au}$ (a) and $\text{Fe}_3\text{O}_4\text{@Au-Apt}$ NCs (b) dispersed in the solution before and after magnet separation. Both of them can be separated from the solution in 15 s with an external magnet. Besides, 4-MBA was used to compare the SERS signal absorbed on surfaces of $\text{Fe}_3\text{O}_4\text{@Au-Apt}$ NCs and $\text{Fe}_3\text{O}_4\text{@Au}$ NCs under the same conditions. The intensity of SERS signals of 4-MBA is almost identical, as displayed in Fig. S4. It can be confirmed from the result that aptamer has almost no effect on magnetic properties and SERS sensitivity of $\text{Fe}_3\text{O}_4\text{@Au}$ NCs.

3.5. Capability of $\text{Fe}_3\text{O}_4\text{@Au-Apt}$ NCs to capture *S. aureus*

The following experiment was performed to evaluate the ability of $\text{Fe}_3\text{O}_4\text{@Au-Apt}$ NCs to capture *S. aureus*. 100 μL (0.1 mg/mL) of $\text{Fe}_3\text{O}_4\text{@Au-Apt}$ NCs was added to 50 μL of *S. aureus* (10^7 cfu/mL) suspensions in PBS buffer. After incubation for 25 min, $\text{Fe}_3\text{O}_4\text{@Au-Apt-S. aureus}$ complex was enriched by using a magnet and supernatant solution was maintained. Subsequently, Supernatant after dilution in equal proportion was coated on LB agar plate by spread plate coating method and incubated overnight at 37 °C. The same experimental procedure was carried out on $\text{Fe}_3\text{O}_4\text{@Au}$ NCs for comparison. The photographs of the LB agar plates in Fig. S5(A) indicate that most of *S. aureus* are captured by $\text{Fe}_3\text{O}_4\text{@Au-Apt}$ NCs. The capture effect can also be evaluated by calculating the cell capture efficiency (CCE). As depicted in Fig. S5(B), OD_{600} values of the *S. aureus* solution and supernatant solution after being incubated with $\text{Fe}_3\text{O}_4\text{@Au}$ NCs and $\text{Fe}_3\text{O}_4\text{@Au-Apt}$ NCs are 0.6, 0.53 and 0.19, respectively. The cell capture efficiency is calculated based on formula $\text{CCE} [\%] = 100\%[a-b]/a$, a and b

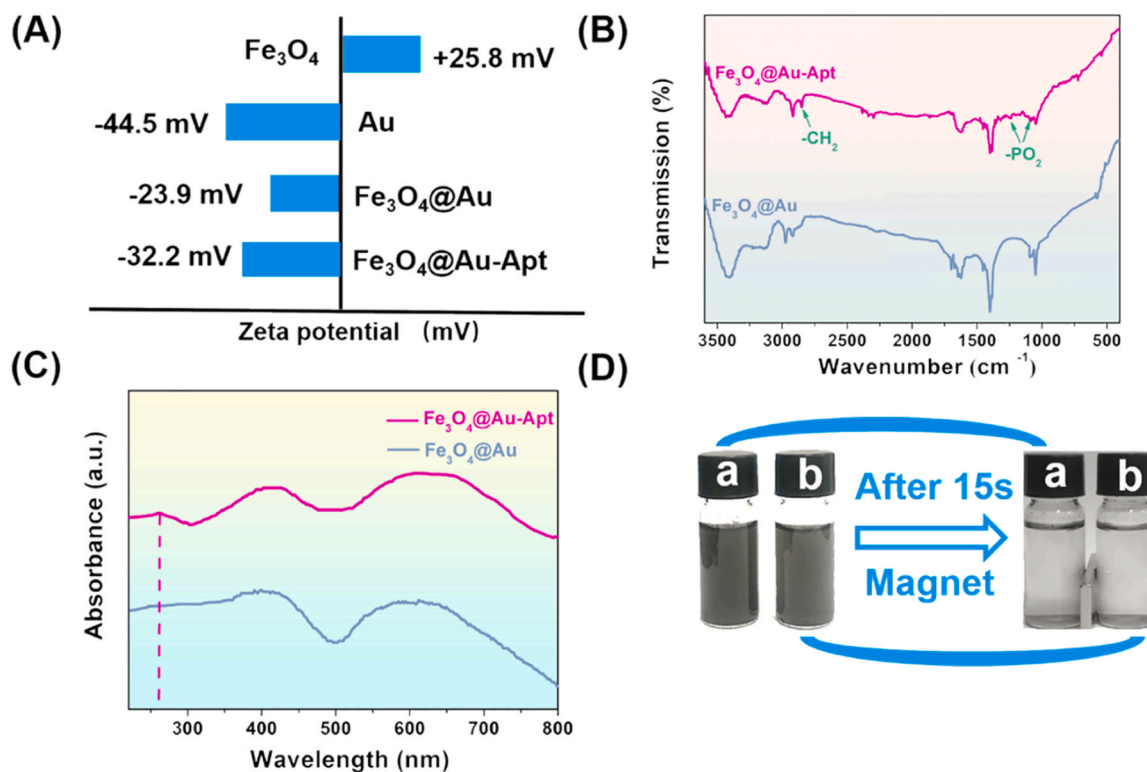


Fig. 2. (A) Zeta potential values of Fe_3O_4 NPs, Au NPs, $\text{Fe}_3\text{O}_4\text{@Au}$ NCs and $\text{Fe}_3\text{O}_4\text{@Au-Apt}$ NCs, (B) FTIR, (C) UV-Vis spectra and (D) magnetic separation test of (a) $\text{Fe}_3\text{O}_4\text{@Au}$ NCs and (b) $\text{Fe}_3\text{O}_4\text{@Au-Apt}$ NCs.

represent OD₆₀₀ value before and after magnetic separation, respectively [62]. Result shows that the CCE of Fe₃O₄@Au-Apt NCs is as high as 68% and is greater than that of Fe₃O₄@Au NCs, indicating that Fe₃O₄@Au-Apt NCs exhibit extraordinary ability to capture *S. aureus*. The binding ability of Fe₃O₄@Au-Apt aptasensor to *S. aureus* was also studied by SEM, and the pretreatment process of samples before SEM analysis was presented in the Supporting Information. The SEM image of *S. aureus* is shown in Fig. 3(A), and the size of *S. aureus* is about 1 μm. The image in Fig. 3(B) shows Fe₃O₄@Au-Apt NCs are well dispersed on the surfaces of *S. aureus*, indicating that Fe₃O₄@Au-Apt NCs have the strong binding force to *S. aureus*. The inset of Fig. 3(B) shows the model of Fe₃O₄@Au-Apt-*S. aureus* complex. SEM-EDS spectrum and EDS elemental mapping images of Fe₃O₄@Au-Apt-*S. aureus* complex in Fig. 3 (C) and (D) display the element composition and distribution in the Fe₃O₄@Au-Apt-*S. aureus* complex. It can be seen that except for Au, O, Fe elements belonging to Fe₃O₄@Au NCs, the principal elements of aptamer including C, N and P are evenly distributed on surfaces of Fe₃O₄@Au NCs [63].

3.6. Optimization of Fe₃O₄@Au-Apt aptasensor and *S. aureus* SERS detection

To establish an optimal aptasensor, the experimental parameters including the concentration of aptamer, the incubation time between the aptamer and Fe₃O₄@Au NCs and the incubation time between the target bacteria and Fe₃O₄@Au-Apt aptasensor were optimized. The SERS spectrum of *S. aureus* based on Fe₃O₄@Au-Apt aptasensor was recorded by the Raman spectrometer present in Fig. S6. Three characteristic Raman peaks of *S. aureus* are observed at 1007, 1158 and 1525 cm⁻¹, where the peak at 1007 cm⁻¹ is attributed to phenylalanine, and other peaks at 1158 and 1525 cm⁻¹ are ascribed to C-C stretch vibration and C=C stretch vibration from β-carotene, respectively [64,65]. Notably, the absence of SERS peak at 735 cm⁻¹ is related to respiration pattern of the adenine ring, indicating that the native DNA rather than denatured DNA contributes to spectra [66]. The intensity of strongest Raman peak at 1525 cm⁻¹ was chosen as reference to optimize experimental parameters. Fig. 4(A) shows that the SERS intensity at 1525 cm⁻¹ increases when the concentration of aptamer increases from 10⁻⁸ M to 10⁻⁴ M. As aptamer concentration further increases to 10⁻³ M, the signal intensity maintains steady, suggesting that the amount of aptamer (10⁻⁴ M) on surfaces of Fe₃O₄@Au NCs reaches saturation and 10⁻⁴ M can be identified as the optimal concentration of aptamer. On the basis of above

experiments, the effect of incubation time on SERS signal intensities of *S. aureus* was also investigated, as presented in Fig. 4(B). As the incubation time increased from 8 to 48 h, SERS intensity of *S. aureus* at 1525 cm⁻¹ increases first, and then decreases and reaches maximum at 24 h. A possible explanation is that the aptamer cannot be immobilized adequately on surfaces of Fe₃O₄@Au NCs within a short incubation time, but the prolonged incubation time can lead to the disconnection of aptamer molecules from surfaces of Fe₃O₄@Au NCs. Therefore, the optimal incubation time between aptamer and Fe₃O₄@Au NCs in this experiment is 24 h. Moreover, the incubation time between *S. aureus* and Fe₃O₄@Au-Apt aptasensor was also optimized. It is found from Fig. S7 that when the incubation time is too long or too short, it is not conducive to enhancing the SERS signal of *S. aureus*. Accordingly, 25 min was regarded as the best incubation time to detect *S. aureus*. Under optimal conditions, SERS spectra of *S. aureus* with different concentrations ranging from 10² to 10⁷ cfu/mL were obtained depicted in Fig. 4(C). Fe₃O₄@Au-Apt aptasensor can detect *S. aureus* as low as 10² cfu/mL. For making a quantitative SERS analysis on *S. aureus*, the corresponding plot of the SERS intensity and logarithmic concentration of *S. aureus* at 1525 cm⁻¹ were fitted. A good linear relationship between SERS intensity and the logarithm of concentration of *S. aureus* can be observed in Fig. 4(D). The linear regression equation is expressed as $y = 235.15x + 171.87$ with corresponding correlation coefficient (R^2) of 0.997. Subsequently, we performed SERS detection on low concentrations of *S. aureus* (15, 25, 35, 45, 55 and 65 cfu/mL) shown in Fig. S8. It can be found that even at a concentration of 25 cfu/mL, the SERS intensity of *S. aureus* is still higher than threshold. Therefore, the limit of detection (LOD) for *S. aureus* can be as low as 25 cfu/mL. The threshold value is calculated by adding three times the standard deviation of blank sample to average intensity [50]. A comparison of results with the reported literature is displayed in Table 1, which discloses that our proposed label-free Fe₃O₄@Au-Apt aptasensor possesses the superiority of high sensitivity, time saving and simple operation.

3.7. Evaluation of selectivity, stability of Fe₃O₄@Au-Apt aptasensor and practical application

The specificity of the Fe₃O₄@Au-Apt aptasensor for *S. aureus* SERS detection is investigated. Several Gram-positive and Gram-negative bacteria including *Escherichia coli*, *Bacillus cereus*, *Vibrio parahaemolyticus*, *Salmonella typhimurium* and *Shigella dysenteriae* were selected as the interfering substances and the concentration of all the

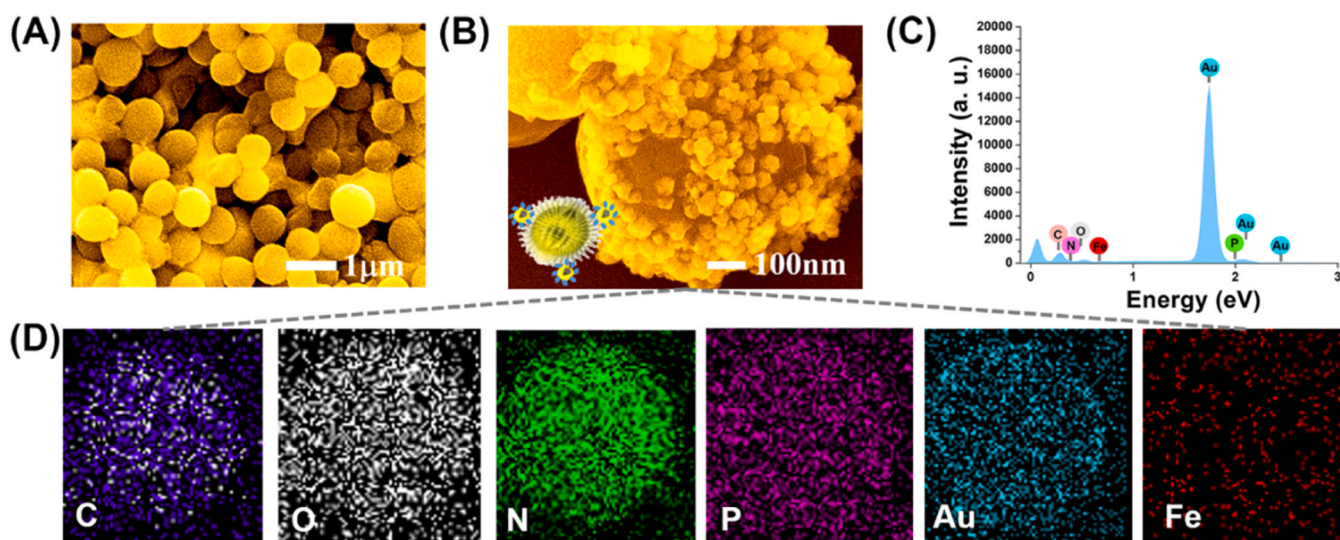


Fig. 3. (A) SEM images of *S. aureus*, (B) SEM images of Fe₃O₄@Au-Apt-*S. aureus* complex, (C) SEM-EDS spectrum and (D) EDS elemental mapping images of Fe₃O₄@Au-Apt-*S. aureus* complex (C, O, N, P, Au, and Fe).

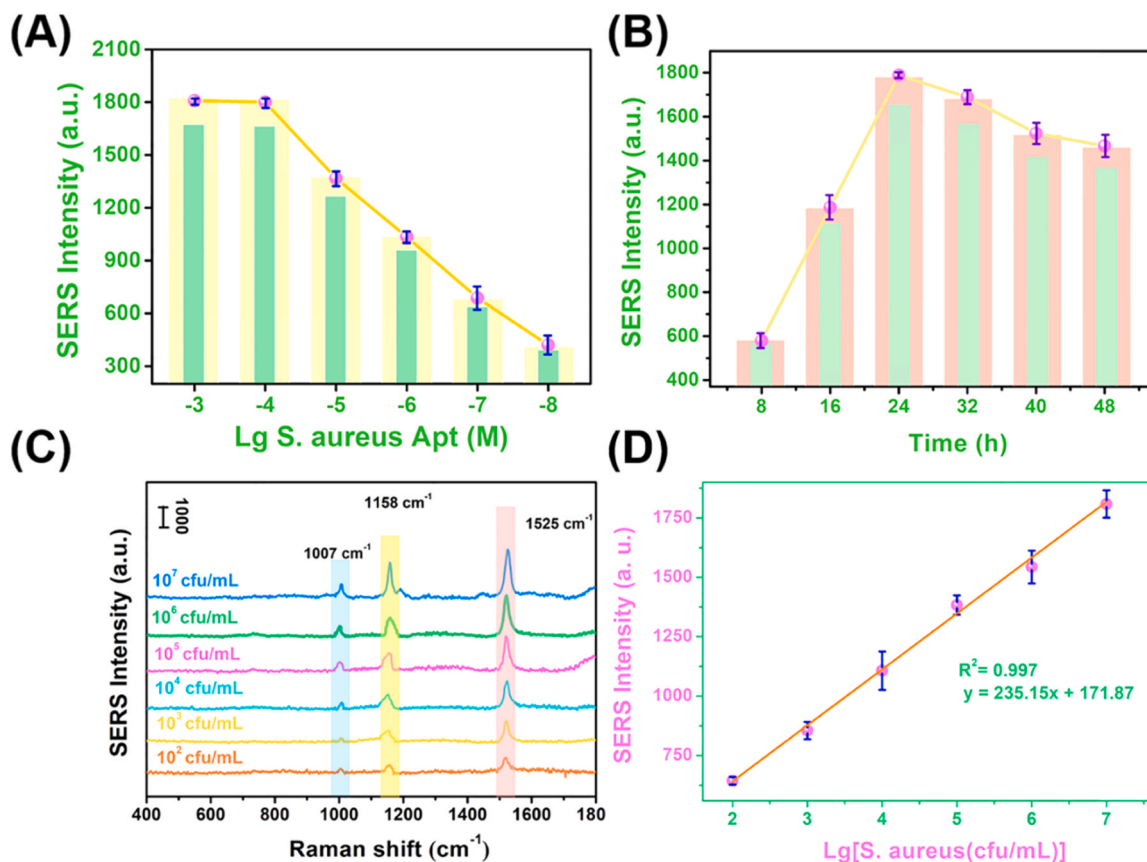


Fig. 4. SERS signal intensities of *S. aureus* at 1525 cm⁻¹ based on Fe₃O₄@Au-Apt NCs at different (A) concentrations of aptamer and (B) incubation time, (C) SERS spectra with different concentrations of *S. aureus* from 10² to 10⁷ cfu/mL and (D) the corresponding plot of SERS intensity and logarithmic concentration of *S. aureus* at 1525 cm⁻¹. The error bars represent the standard deviations from three measurements.

Table 1

Overall performance of Fe₃O₄@Au-Apt aptasensor compared with other reports.

Detection method/ recognition element	LOD (cfu/ mL)	Signal reporter	Total time	Reference
SERS/boric acid	100	Silicon wafer decorated with AgNPs/4-MPBA	20 min	[67]
SERS/Apt	35	Au@DTNB	70 min	[21]
SERS/AMP	10	Au@Ag-GO/4-MPBA	over 16 h	[68]
Fluorescence bioassays/Apt	20	multicolor lanthanide- doped time-resolved fluorescence NPs	over 40 min	[69]
SERS/Apt	25	Label-free	30 min	this work

bacterial samples was set as 10⁷ cfu/mL. Fig. 5(A) shows that as compared with other bacterial samples, SERS signal intensity of *S. aureus* is higher. On the basis of this finding, it can be concluded that the Fe₃O₄@Au-Apt aptasensor has a strong ability to discriminate and bind the target molecules (*S. aureus*). The stability of the Fe₃O₄@Au-Apt aptasensor was demonstrated based on the reproducibility of SERS signal. Fe₃O₄@Au-Apt NCs were stored for 12 days and *S. aureus* was detected under same conditions every 3 days. The SERS intensity of *S. aureus* on the Fe₃O₄@Au-Apt NCs still maintains almost unchanged within 12 days as depicted in Fig. 5(B), manifesting the excellent stability of the proposed SERS aptasensor. The reproducibility and uniformity of the SERS signal on the Fe₃O₄@Au-Apt NCs were also investigated. In order to obtain the SERS spectrum of *S. aureus* (10⁶ cfu/mL), 10 locations were randomly selected from the same batch of Fe₃O₄@Au-Apt NCs. As can be seen in Fig. S9(A) and (B), it is no significant

change in the shape and characteristic peak intensity of all SERS spectra, and the relative standard deviation (RSD) is about 7.8%. Subsequently, the intensities of the SERS peak of *S. aureus* at 1525 cm⁻¹ measured on different batches of Fe₃O₄@Au-Apt NCs were studied in Fig. S9(C), and the RSD was calculated to be 8.7%. Furthermore, in order to assess the practicality, Fe₃O₄@Au-Apt aptasensor was used to detect *S. aureus* in real food samples. *S. aureus* with different concentrations (about 10², 10³, and 10⁴ cfu/mL) were spiked with three portions of milk samples, respectively. After Fe₃O₄@Au-Apt NCs were reacted with the milk samples for 25 min, the complex was separated with magnet and washed for 5 times. Finally, Fe₃O₄@Au-Apt-*S. aureus* complex was transferred to a glass slide for SERS measurement. Detailed process of SERS detection in milk samples is exhibited in Fig. S10(A). Fig. S10(B) shows the photographs and SERS signals of *S. aureus* in milk samples. Both SERS method and the classic plate counting method were used to evaluate the number of *S. aureus*. Results in Table S1 indicate that the number of *S. aureus* is almost same by the two methods, which demonstrates the universal applicability and accuracy of Fe₃O₄@Au-Apt aptasensor to detect *S. aureus* in real samples.

3.8. Evaluation of in vitro photothermal conversion effect of Fe₃O₄@Au-Apt aptasensor

The elimination of bacteria at an early stage is the key to inhibiting the further growth and reproduction of bacteria. Given that Fe₃O₄@Au-Apt NCs exhibit strong plasmon resonance absorption in short-wavelength NIR region (Fig. 2(C)) and thus possess potential photothermal conversion characteristics, the photothermal performance of Fe₃O₄@Au-Apt NCs was tested by 808 nm laser (1.5 W cm⁻²) [70]. As depicted in Fig. 6(A), temperature of Fe₃O₄@Au-Apt NCs (200 μg/mL)

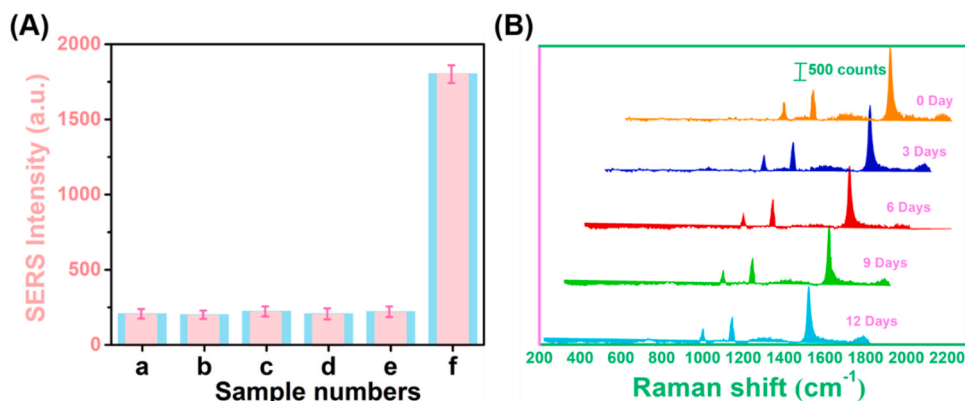


Fig. 5. (A) The specific result of detecting of *S. aureus*, a-f: *Escherichia coli*, *Bacillus cereus*, *Vibrio parahaemolyticus*, *Salmonella typhimurium*, *Shigella dysenteriae* and *S. aureus*. (B) SERS spectra of *S. aureus* based on Fe_3O_4 @Au-Apt NCs stored for 12 days. The error bars show the standard deviation of three replicate determinations.

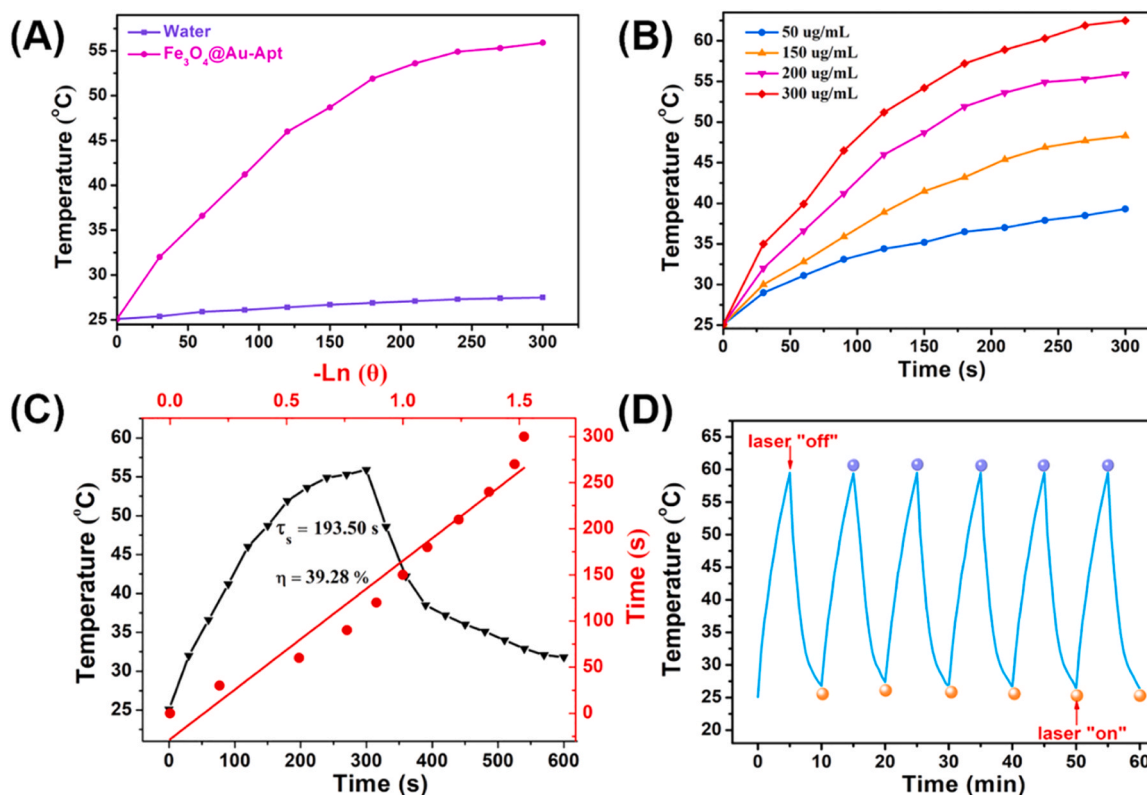


Fig. 6. (A) Temperature varied of Fe_3O_4 @Au-Apt NCs (200 $\mu\text{g}/\text{mL}$) and water control samples under irradiation for 5 min, (B) heating curves of Fe_3O_4 @Au-Apt NCs with different concentrations (50, 150, 200, 300 $\mu\text{g}/\text{mL}$) under irradiation for 5 min, (C) calculation of η of Fe_3O_4 @Au-Apt NCs (200 $\mu\text{g}/\text{mL}$) and (D) cyclic temperature profiles of Fe_3O_4 @Au-Apt NCs with concentration of 200 $\mu\text{g}/\text{mL}$ over six laser-on/off cycles.

increases significantly under 808 nm laser irradiation and maintains stable after 5 min (55.9 °C), while the temperature of water as control sample has not risen dramatically. The changes in temperature make us conclude that Fe_3O_4 @Au-Apt NCs can convert 808 nm laser energy into heat energy quickly and effectively. The reason is that the free electrons of plasmonic Au NPs on surfaces of Fe_3O_4 @Au-Apt NCs can undergo coherent oscillation under laser excitation. The amplitude of the oscillation will reach a maximum when the frequency of light is equal to the vibration frequency of the atom [71]. The generated energy is converted to heat through the light oscillation of the oscillating electrons and transferred to the Fe_3O_4 @Au-Apt NCs through the electron-phonon relaxation [72]. The heat released from Fe_3O_4 @Au-Apt NCs generated by phonon-phonon reaction increases the ambient temperature. In addition, this was demonstrated in a number of studies that the

photothermal behavior was closely related to the concentration of plasmonic metal NCs. Fig. 6(B) presents that temperature increases with the increased concentration of Fe_3O_4 @Au-Apt NCs. When the concentration of Fe_3O_4 @Au-Apt NCs is 300 $\mu\text{g}/\text{mL}$, the temperature increases to 64.8 °C after 5 min. It has been proved that the temperature above 50 °C can result in the death of bacteria [73,74]. However, excessive temperatures (> 60 °C) may cause significant toxicity to healthy tissues [75]. Therefore, 200 $\mu\text{g}/\text{mL}$ of Fe_3O_4 @Au-Apt NCs is chosen as the preferred concentration in the next experiments because it can effectively kill bacteria and minimize damage to normal tissues. The photothermal conversion efficiency (η) of Fe_3O_4 @Au-Apt NCs was calculated on the previous methods, and the η value was estimated by the following Eq. (1): [76,77].

$$\eta = \frac{hS(T_{max} - T_{surr}) - Q_{Dis}}{I(1 - 10^{-A_i})} \quad (1)$$

where I is incident energy of 808 nm laser and A_i is the absorbance of $Fe_3O_4@Au$ -Apt NCs at 808 nm. Then, hS can be calculated by Eq. (2), and m and C_p are the mass (0.4 g) and heat capacity (4.2 J g⁻¹) of water, respectively.

$$hS = \frac{\sum mC_p}{\tau_s} \quad (2)$$

τ_s , an unknown value can be obtained by following equations. First, a dimensionless quantity θ needs to be defined, corresponding to Eq. (3).

$$\theta = \frac{T - T_{surr}}{T_{max} - T_{surr}} \quad (3)$$

T , T_{surr} and T_{max} represent the solution temperature, the ambient temperature (25.1 °C) and the equilibrium temperature after 5 min irradiation (55.9 °C), respectively. The time constant τ_s can be determined by linear fitting using the cooling time of the natural cooling stage (between 300 s and 600 s) and the negative natural logarithm of θ according to Eqs. (4) and (5). As plotted in Fig. 6(C), the slope value is τ_s and the τ_s and hS is 193.50 s and 8.7 mW/°C, respectively.

$$t = -\tau_s \ln \frac{T - T_{surr}}{T_{max} - T_{surr}} \quad (4)$$

$$t = -\tau_s \ln \theta \quad (5)$$

In this work, I is 1.17 W (1.5 W cm⁻², spot diameter = 10 mm) and A_{808} is 0.38. Q_{Dis} is the heat dissipation in the light absorption of 96-well plate and it is so small that it can be ignored. Finally, after substituting all parameter values into Eq. (1), the η of $Fe_3O_4@Au$ -Apt NCs is calculated to be 39.28%, which is higher than that in the previous reports [78–80]. The real-time photothermal images of Au NPs and $Fe_3O_4@Au$ -Apt NCs after 808 nm laser irradiation with intervals of 30 s were present in Fig. S11(A). η value of Au NPs was also calculated in the Supporting Information (Fig. S11(B)). The temperature of $Fe_3O_4@Au$ -Apt NCs increased by 30.8 °C within 5 min, which is much higher than Au NPs (7.9 °C). The η value of $Fe_3O_4@Au$ -Apt NCs (39.28%) is higher than Au NPs (12.9%). This may attribute to the strong absorption of NIR light caused by the LSPR of Au shell in the NIR region [81,82]. The photothermal stability of the $Fe_3O_4@Au$ -Apt NCs was also investigated, as presented in Fig. 6(D). After six cycles, the highest temperature of solution containing $Fe_3O_4@Au$ -Apt NCs only drops by 0.3 °C. These results prove that $Fe_3O_4@Au$ -Apt NCs have high photothermal conversion efficiency and possess excellent photothermal stability.

3.9. In vitro NIR PTT of *S. aureus* by $Fe_3O_4@Au$ -Apt aptasensor

On the basis of the excellent NIR photothermal performance, $Fe_3O_4@Au$ -Apt aptasensor was chosen for in vitro photothermal treatment of *S. aureus* in milk samples. Process of NIR-triggered PTT for *S. aureus* is illustrated in Scheme 1(C). To study the photothermal effect and cytotoxicity of $Fe_3O_4@Au$ -Apt NCs to *S. aureus*, *S. aureus* suspensions were divided into four groups: (i) an untreated *S. aureus* group (Fig. 7(a) and (e)), (ii) a group treated with NIR laser (808 nm, 1.5 W cm⁻²) for 5 min to inactivate *S. aureus* (Fig. 7(b) and (f)), (iii) a group with $Fe_3O_4@Au$ -Apt NCs (Fig. 7(c) and (g)) and (iv) a group with both $Fe_3O_4@Au$ -Apt NCs and NIR laser (Fig. 7(d) and (h)). Live *S. aureus* was stained with Calcein-AM dye and generated green fluorescence and dead *S. aureus* was stained with PI and produced bright red fluorescence [83]. When *S. aureus* is incubated only with $Fe_3O_4@Au$ -Apt NCs or is irradiated only by NIR light, green fluorescence can be observed, indicating that *S. aureus* is still alive. This result also suggests indirectly that the cytotoxicity of $Fe_3O_4@Au$ -Apt NCs to *S. aureus* is negligible. In contrast, the combined effects of $Fe_3O_4@Au$ -Apt NCs and NIR irradiation can lead to inactivation of *S. aureus* owing to the change of color in fluorescence from green to red. This may be explained by the sterilization mechanism of PTT. When *S. aureus* is incubated with $Fe_3O_4@Au$ -Apt NCs, the aptamer enables $Fe_3O_4@Au$ -Apt NCs to specifically recognize and capture the target bacteria. After being irradiated by the NIR laser, the local heat generated by $Fe_3O_4@Au$ -Apt NCs with NIR photothermal conversion ability directly acts on the *S. aureus*, which may destroy the bacterial membrane, cause the increase in its permeability, denature proteins and enzymes, and eventually lead to dead *S. aureus* [75]. Besides, in order to calculate the sterilization rate, the number of colonies on the agar plate was counted shown in Fig. S12. The survival numbers of bacteria after four different treatments are 993, 960, 923, and 25 respectively. The sterilization rate of $Fe_3O_4@Au$ -Apt NCs combined with laser is as high as 97%, which demonstrates that $Fe_3O_4@Au$ -Apt NCs have great potential in killing bacteria in food.

4. Conclusions

In conclusion, a rapid, sensitive and stable $Fe_3O_4@Au$ -Apt aptasensor has been demonstrated for capture, SERS detection and photothermal killing of *S. aureus*. SERS enhancement mechanism of $Fe_3O_4@Au$ NCs is discussed by using 4-MBA as a probe molecule. $Fe_3O_4@Au$ -Apt aptasensor has outstanding ability (68%) to capture *S. aureus* after surface modification of $Fe_3O_4@Au$ NCs with nucleic acid aptamer. By recording the SERS intensity of different aptamer concentrations and incubation time, we can get the optimal $Fe_3O_4@Au$ -Apt aptasensor (10⁻⁴ M for aptamer, 24 h for incubation time between aptamer and $Fe_3O_4@Au$ NCs and 25 min for incubation time between

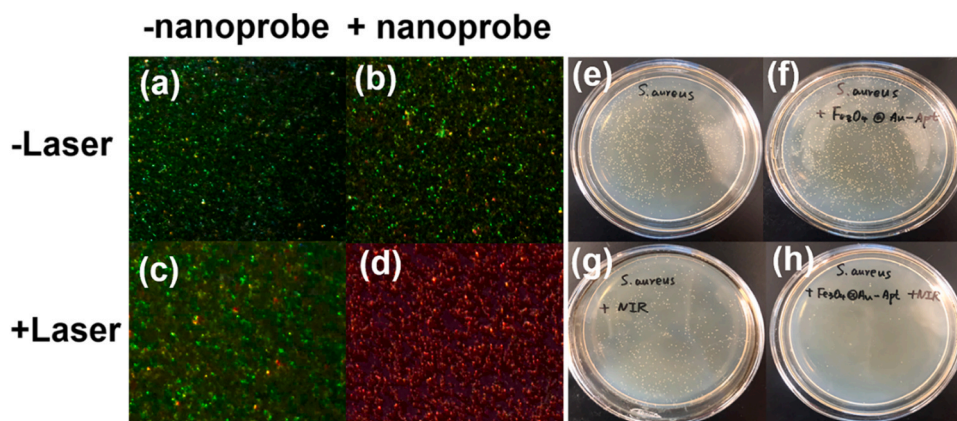


Fig. 7. Live and dead fluorescence images (left) and photographs of the colony numbers (right) after processing *S. aureus* in milk samples treated with (a, e) none, (b, f) only $Fe_3O_4@Au$ -Apt NCs, (c, g) only NIR laser and (d, h) both $Fe_3O_4@Au$ -Apt NCs and NIR laser.

target bacteria and aptasensor). A good linear relationship is found between SERS intensity and logarithm of *S. aureus* concentration between 10^2 to 10^7 cfu/mL ($y = 235.15x + 171.87$, $R^2 = 0.997$), and the LOD for *S. aureus* is 25 cfu/mL. Compared with other reported methods, the developed $\text{Fe}_3\text{O}_4/\text{Au}$ -Apt aptasensor has the advantages of simplicity, sensitivity, and short analysis time (only 30 min). $\text{Fe}_3\text{O}_4/\text{Au}$ -Apt aptasensor exhibits high photothermal conversion efficiency (39.28%) during the photothermal treatment process, thereby achieving effective killing of *S. aureus*. In addition, $\text{Fe}_3\text{O}_4/\text{Au}$ -Apt aptasensor can detect and kill *S. aureus* in milk samples and shows high biocompatibility and negligible cytotoxicity under NIR irradiation, which confirms that it can be used for detecting and inactivating bacteria in food samples. This work not only provides a new avenue to develop multifunctional aptasensors in capture, sensitive detection and treatment of pathogen, but also provides a potential platform in a wide variety of applications in clinical treatment and diagnosis.

CRedit authorship contribution statement

Wenshi Zhao: Data curation, Writing – original draft, Investigation, Writing – review & editing. **Daxin Zhang:** Investigation. **Tianxiang Zhou:** Formal analysis, Investigation. **Jie Huang:** Software. **Yushan Wang:** Conceptualization. **Boxun Li:** Data curation. **Lei Chen:** Methodology. **Jinghai Yang:** Resources, Supervision. **Yang Liu:** Conceptualization, Resources, Supervision.

Declaration of Competing Interest

The authors declare that they have no known competing financial interests or personal relationships that could have appeared to influence the work reported in this paper.

Acknowledgements

This work was funded by the National Natural Science Foundation of China, China (Grant Numbers 21676115), Program for the development of Science and Technology of Jilin province, China (Grant Numbers 20200301043RQ and 20190103002JH) and Program for Science and Technology of Education Department of Jilin Province, China (Grant Numbers JJKH20200418KJ).

Appendix A. Supporting information

Supplementary data associated with this article can be found in the online version at [doi:10.1016/j.snb.2021.130879](https://doi.org/10.1016/j.snb.2021.130879).

References

- L. Chen, Y.K. Leng, B. Liu, J. Liu, S.P. Wan, T. Wu, et al., Ultrahigh-sensitivity label-free optical fiber biosensor based on a tapered singlemode-no core-singlemode coupler for *Staphylococcus aureus* detection, *Sens. Actuators B-Chem.* 320 (2020), 128283, <https://doi.org/10.1016/j.snb.2020.128283>.
- M. Shahdordizadeh, S.M. Taghdisi, N. Ansari, F.A. Langroodi, K. Abnous, M. Ramezani, Aptamer based biosensors for detection of *Staphylococcus aureus*, *Sens. Actuators B-Chem.* 241 (2017) 619–635, <https://doi.org/10.1016/j.snb.2016.10.088>.
- M. Zhang, H. Zhang, J. Feng, Y. Zhou, B. Wang, Synergistic chemotherapy, physiotherapy and photothermal therapy against bacterial and biofilms infections through construction of chiral glutamic acid functionalized gold nanobipyramids, *Chem. Eng. J.* 393 (2020), 124778, <https://doi.org/10.1016/j.cej.2020.124778>.
- S. Juneja, J. Bhattacharya, Coffee ring effect assisted improved *S. aureus* screening on a physically restrained gold nanoflower enriched SERS substrate, *Colloid Surf. B* 182 (2019), 110349, <https://doi.org/10.1016/j.colsurfb.2019.110349>.
- J. Wang, X. Wu, C. Wang, Z. Rong, H. Ding, H. Li, et al., Facile synthesis of Au-coated magnetic nanoparticles and their application in bacteria detection via a SERS method, *ACS Appl. Mater. Interfaces* 8 (2016) 19958–19967, <https://doi.org/10.1021/acsami.6b07528>.
- C. Wang, J. Wang, M. Li, X. Qu, K. Zhang, Z. Rong, et al., A rapid SERS method for label-free bacteria detection using polyethylenimine-modified Au-coated magnetic microspheres and Au@Ag nanoparticles, *Analyst* 141 (2016) 6226–6238, <https://doi.org/10.1039/c6an01105e>.
- H. Wang, H.C. Koydemir, Y. Qiu, B. Bai, Y. Zhang, Y. Jin, et al., Early detection and classification of live bacteria using time-lapse coherent imaging and deep learning, *Light Sci. Appl.* 9 (2020) 118, <https://doi.org/10.1038/s41377-020-00358-9>.
- X. Gao, H. Wu, Z. Hao, X. Ji, X. Lin, S. Wang, Y. Liu, A multifunctional plasmonic chip for bacteria capture, imaging, detection, and in-situ elimination for wound therapy, *Nanoscale* 12 (2020) 6489–6497, <https://doi.org/10.1039/D0NR00638F>.
- M.G. Rizzo, S. Carnazza, L.M. De Plano, D. Franco, M.S. Nicolò, V. Zammuto, et al., Rapid detection of bacterial pathogens in blood through engineered phages-beads and integrated Real-Time PCR into MicroChip, *Sens. Actuators B-Chem.* 329 (2021), 129227, <https://doi.org/10.1016/j.snb.2020.129227>.
- S. Hameed, L. Xie, Y. Ying, Conventional and emerging detection techniques for pathogenic bacteria in food science: a review, *Trends Food Sci. Technol.* 81 (2018) 61–73, <https://doi.org/10.1016/j.tifs.2018.05.020>.
- K. Whang, J.H. Lee, Y. Shin, W. Lee, Y.W. Kim, D. Kim, et al., Plasmonic bacteria on a nanoporous mirror via hydrodynamic trapping for rapid identification of waterborne pathogens, *Light Sci. Appl.* 7 (2018) 68, <https://doi.org/10.1038/s41377-018-0071-4>.
- M. Majdinasab, A. Hayat, J.L. Marty, Aptamer-based assays and aptasensors for detection of pathogenic bacteria in food samples, *TRAC Trend Anal. Chem.* 107 (2018) 60–77, <https://doi.org/10.1016/j.trac.2018.07.016>.
- A. Zhu, S. Ali, Y. Xu, Q. Ouyang, Q. Chen, A SERS aptasensor based on AuNPs functionalized PDMS film for selective and sensitive detection of *Staphylococcus aureus*, *Biosens. Bioelectron.* 172 (2021), 112806, <https://doi.org/10.1016/j.bios.2020.112806>.
- S. Yan, R. An, Y. Zou, N. Yang, Y. Zhang, Fabrication of polymer colloidal/Au composite nanofilms for stable and reusable SERS-active substrates with highly-dense hotspots, *Sens. Actuators B-Chem.* 302 (2020), 127107, <https://doi.org/10.1016/j.snb.2019.127107>.
- X. Liu, X. Yang, K. Li, H. Liu, R. Xiao, W. Wang, et al., $\text{Fe}_3\text{O}_4/\text{Au}$ SERS tags-based lateral flow assay for simultaneous detection of serum amyloid A and C-reactive protein in unprocessed blood sample, *Sens. Actuators B-Chem.* 320 (2020), 128350, <https://doi.org/10.1016/j.snb.2020.128350>.
- Y. Xu, F.Y.H. Kutsanedzie, M.M. Hassan, J. Zhu, H. Li, Q. Chen, Functionalized hollow Au@Ag nanoflower SERS matrix for pesticide sensing in food, *Sens. Actuators B-Chem.* 324 (2020), 128718, <https://doi.org/10.1016/j.snb.2020.128718>.
- M. Muhammad, C.S. Shao, Q. Huang, Aptamer-functionalized Au nanoparticles array as the effective SERS biosensor for label-free detection of interleukin-6 in serum, *Sens. Actuators B-Chem.* 334 (2021), 129607, <https://doi.org/10.1016/j.snb.2021.129607>.
- S. Yang, J. Yao, Y. Quan, M. Hu, R. Su, M. Gao, et al., Monitoring the charge-transfer process in a Nd-doped semiconductor based on photoluminescence and SERS technology, *Light Sci. Appl.* 9 (2020), <https://doi.org/10.1038/s41377-020-00361-0>.
- Q. He, Y. Han, Y. Huang, J. Gao, Y. Gao, L. Han, et al., Reusable dual-enhancement SERS sensor based on graphene and hybrid nanostructures for ultrasensitive lead (II) detection, *Sens. Actuators B-Chem.* 341 (2021), 130031, <https://doi.org/10.1016/j.snb.2021.130031>.
- H. Zhou, D. Yang, N.E. Mircescu, N.P. Ivleva, K. Schwarzmeier, A. Wieser, S. Schubert, R. Niessner, C. Haisch, Surface-enhanced Raman scattering detection of bacteria on microarrays at single cell levels using silver nanoparticles, *Microchim. Acta* 182 (2015) 2259–2266, <https://doi.org/10.1007/s00604-015-1570-0>.
- H. Zhang, X. Ma, Y. Liu, N. Duan, S. Wu, Z. Wang, et al., Gold nanoparticles enhanced SERS aptasensor for the simultaneous detection of *Salmonella typhimurium* and *Staphylococcus aureus*, *Biosens. Bioelectron.* 74 (2015) 872–877, <https://doi.org/10.1016/j.bios.2015.07.033>.
- C. Zhang, C. Wang, R. Xiao, L. Tang, J. Huang, D. Wu, et al., Sensitive and specific detection of clinical bacteria via vancomycin-modified $\text{Fe}_3\text{O}_4/\text{Au}$ nanoparticles and aptamer-functionalized SERS tags, *J. Mater. Chem. B* 6 (2018) 3751–3761, <https://doi.org/10.1039/c8tb00504d>.
- X.S. Zheng, I.J. Jahn, K. Weber, D.C. May, J. Popp, Label-free SERS in biological and biomedical applications: recent progress, current challenges and opportunities, *Spectrochim. Acta A* 197 (2018) 56–77, <https://doi.org/10.1016/j.saa.2018.01.063>.
- X. Chen, M. Tang, Y. Liu, J. Huang, Z. Liu, H. Tian, et al., Surface-enhanced Raman scattering method for the identification of methicillin-resistant *Staphylococcus aureus* using positively charged silver nanoparticles, *Microchim. Acta* 186 (2019) 102, <https://doi.org/10.1007/s00604-018-3150-6>.
- H. Zhang, S. Huang, X. Yang, R. Yuan, Y. Chai, A SERS biosensor constructed by calcined ZnO substrate with high-efficiency charge transfer for sensitive detection of Pb^{2+} , *Sens. Actuators B-Chem.* 343 (2021), 130142, <https://doi.org/10.1016/j.snb.2021.130142>.
- A.A. Kowalska, A. Kaminska, W. Adamkiewicz, E. Witkowska, M. Tkacz, Novel highly sensitive Cu-based SERS platforms for biosensing applications, *J. Raman Spectrosc.* 46 (2015) 428–433, <https://doi.org/10.1002/jrs.4674>.
- E.J.C. Dias, R. Yu, F.J. Garcia de Abajo, Thermal manipulation of plasmons in atomically thin films, *Light Sci. Appl.* 9 (2020) 87, <https://doi.org/10.1038/s41377-020-0322-z>.
- L. Lu, Y. Ge, X. Wang, Z. Lu, T. Wang, H. Zhang, et al., Rapid and sensitive multimode detection of *Salmonella typhimurium* based on the photothermal effect and peroxidase-like activity of MoS_2/Au nanocomposite, *Sens. Actuators B-Chem.* 326 (2021), 128807, <https://doi.org/10.1016/j.snb.2020.128807>.
- S. Kaushal, N. Priyadarshi, A.K. Pinnaka, S. Soni, A. Deep, N.K. Singhal, Glycoconjugates coated gold nanorods based novel biosensor for optical detection

- and photothermal ablation of food borne bacteria, *Sens. Actuators B-Chem.* 289 (2019) 207–215, <https://doi.org/10.1016/j.snb.2019.03.096>.
- [30] Z. Xie, M. Peng, R. Lu, X. Meng, W. Liang, Z. Li, et al., Black phosphorus-based photothermal therapy with aCD47-mediated immune checkpoint blockade for enhanced cancer immunotherapy, *Light Sci. Appl.* 9 (2020) 161, <https://doi.org/10.1038/s41377-020-00388-3>.
- [31] L. Wang, N.J. Long, L. Li, Y. Lu, M. Li, J. Cao, et al., Multi-functional bismuth-doped bioglasses: combining bioactivity and photothermal response for bone tumor treatment and tissue repair, *Light Sci. Appl.* 7 (2018) 1, <https://doi.org/10.1038/s41377-018-0007-z>.
- [32] X. Bao, Y. Yuan, J. Chen, B. Zhang, D. Li, D. Zhou, et al., In vivo theranostics with near-infrared-emitting carbon dots-highly efficient photothermal therapy based on passive targeting after intravenous administration, *Light Sci. Appl.* 7 (2018) 91, <https://doi.org/10.1038/s41377-018-0090-1>.
- [33] S. Wen, X. Miao, G.C. Fan, T. Xu, L.P. Jiang, P. Wu, et al., Aptamer-conjugated Au nanocage/SiO₂ core-shell bifunctional nanoprobes with high stability and biocompatibility for cellular SERS imaging and near-infrared photothermal therapy, *ACS Sens.* 4 (2019) 301–308, <https://doi.org/10.1021/acssensors.8b00682>.
- [34] W.C. Huang, P.J. Tsai, Y.C. Chen, Multifunctional Fe₃O₄@Au nanoeegs as photothermal agents for selective killing of nosocomial and antibiotic-resistant bacteria, *Small* 5 (2009) 51–56, <https://doi.org/10.1002/sml.200801042>.
- [35] S. Rajkumar, M. Prabhakaran, Multi-functional core-shell Fe₃O₄@Au nanoparticles for cancer diagnosis and therapy, *Colloid Surf. B* 174 (2019) 252–259, <https://doi.org/10.1016/j.colsurfb.2018.11.004>.
- [36] D. Song, R. Yang, F. Long, A. Zhu, Applications of magnetic nanoparticles in surface-enhanced Raman scattering (SERS) detection of environmental pollutants, *J. Environ. Sci.* 80 (2019) 14–34, <https://doi.org/10.1016/j.jes.2018.07.004>.
- [37] W.E. Hong, L.L. Hsu, S.Y. Huang, C.W. Lee, H. Ko, P.J. Tsai, et al., Assembled growth of 3D Fe₃O₄@Au nanoparticles for efficient photothermal ablation and SERS detection of microorganisms, *J. Mater. Chem. B* 6 (2018) 5689–5697, <https://doi.org/10.1039/C8TB00599K>.
- [38] H. He, D.W. Sun, H. Pu, L. Huang, Bridging Fe₃O₄@Au nanoflowers and Au@Ag nanospheres with aptamer for ultrasensitive SERS detection of aflatoxin B1, *Food Chem.* 324 (2020), 126832, <https://doi.org/10.1016/j.foodchem.2020.126832>.
- [39] Y. Li, X. Wang, L. Gao, P. Hu, L. Jiang, T. Ren, et al., Aptamer-conjugated gold nanostars for targeted cancer photothermal therapy, *J. Mater. Sci.* 53 (2018) 14138–14148, <https://doi.org/10.1007/s10853-018-2668-7>.
- [40] S. Fang, D. Song, Y. Zhuo, Y. Chen, A. Zhu, F. Long, Simultaneous and sensitive determination of *Escherichia coli* O157:H7 and *Salmonella Typhimurium* using evanescent wave dual-color fluorescence aptasensor based on micro/nano size effect, *Biosens. Bioelectron.* 185 (2021), 113288, <https://doi.org/10.1016/j.bios.2021.113288>.
- [41] S. Zhou, C. Lu, Y. Li, L. Xue, C. Zhao, G. Tian, et al., Gold nanobones enhanced ultrasensitive surface-enhanced Raman scattering aptasensor for detecting *Escherichia coli* O157:H7, *ACS Sens.* 5 (2020) 588–596, <https://doi.org/10.1021/acssensors.9b02600>.
- [42] I. Ocsoy, S. Yusufbeyoglu, V. Yilmaz, E.S. McLamore, N. Ildiz, A. Ulgen, DNA aptamer functionalized gold nanostructures for molecular recognition and photothermal inactivation of methicillin-resistant *Staphylococcus aureus*, *Colloid Surf. B* 159 (2017) 16–22, <https://doi.org/10.1016/j.colsurfb.2017.07.056>.
- [43] Y. Pang, N. Wan, L. Shi, C. Wang, Z. Sun, R. Xiao, et al., Dual-recognition surface-enhanced Raman scattering(SERS)biosensor for pathogenic bacteria detection by using vancomycin-SERS tags and aptamer-Fe₃O₄@Au, *Anal. Chim. Acta* 1077 (2019) 288–296, <https://doi.org/10.1016/j.aca.2019.05.059>.
- [44] A.K. Singh, R. Tiwari, V.K. Singh, P. Singh, S.R. Khadim, U. Singh, et al., Green synthesis of gold nanoparticles from *Dunaliella salina*, its characterization and in vitro anticancer activity on breast cancer cell line, *J. Drug Deliv. Sci. Technol.* 51 (2019) 164–176, <https://doi.org/10.1016/j.jddst.2019.02.023>.
- [45] W. Zhao, S. Yang, C. Guo, J. Yang, Y. Liu, One-step fabrication of Fe₃O₄-Cu nanocomposites: high-efficiency and low-cost catalysts for reduction of 4-nitrophenol, *Mater. Chem. Phys.* 260 (2021), 124144, <https://doi.org/10.1016/j.matchemphys.2020.124144>.
- [46] T. Wu, H. Zheng, Y. Kou, X. Su, N.R. Kadasala, M. Gao, et al., Self-sustainable and recyclable ternary Au@Cu₂O-Ag nanocomposites: application in ultrasensitive SERS detection and highly efficient photocatalysis of organic dyes under visible light, *Microsyst. Nanoeng.* 7 (2021), <https://doi.org/10.1038/s41378-021-00250-5>.
- [47] F. Chang, H. Chen, X. Zhang, B. Lei, X. Hu, N-p heterojunction Bi₄O₅I₂/Fe₃O₄ composites with efficiently magnetic recyclability and enhanced visible-light-driven photocatalytic performance, *Sep. Purif. Technol.* 238 (2020), 116442, <https://doi.org/10.1016/j.seppur.2019.116442>.
- [48] C. Karami, M.A. Taher, A catechol biosensor based on immobilizing laccase to Fe₃O₄@Au core-shell nanoparticles, *Int. J. Biol. Macromol.* 129 (2019) 84–90, <https://doi.org/10.1016/j.ijbiomac.2019.02.015>.
- [49] D.A. Wheeler, S.A. Adams, T. López-Luke, A. Torres-Castro, J.Z. Zhang, Magnetic Fe₃O₄-Au core-shell nanostructures for surface enhanced Raman scattering, *Ann. Phys. -Berlinlin.* 524 (2012) 670–679, <https://doi.org/10.1002/andp.201200161>.
- [50] Y. Kou, T. Wu, H. Zheng, N.R. Kadasala, S. Yang, C. Guo, L. Chen, Y. Liu, J. Yang, Recyclable magnetic MIP-based SERS sensors for selective, sensitive, and reliable detection of paclitaxel residues in complex environments, *ACS Sustain. Chem. Eng.* 8 (2020) 14549–14556, <https://doi.org/10.1021/acsschemeng.0c05065>.
- [51] C. Sun, T. Chen, W. Ruan, B. Zhao, Q. Cong, Controlling the orientation of probe molecules on surface-enhanced Raman scattering substrates: a novel strategy to improve sensitivity, *Anal. Chim. Acta* 994 (2017) 65–72, <https://doi.org/10.1016/j.aca.2017.10.004>.
- [52] W.L.J. Hasi, X. Lin, X.T. Lou, S. Lin, F. Yang, D.Y. Lin, Z.W. Lu, Chloride ion-assisted self-assembly of silver nanoparticles on filter paper as SERS substrate, *Appl. Phys. A-Mater.* 118 (2015) 799–807, <https://doi.org/10.1007/s00339-014-8800-x>.
- [53] W.L.J. Hasi, S. Lin, X. Lin, X.T. Lou, F. Yang, D.Y. Lin, Z.W. Lu, Rapid fabrication of self-assembled interfacial film decorated filter paper as an excellent surface-enhanced Raman scattering substrate, *Anal. Methods* 6 (2014) 9547–9553, <https://doi.org/10.1039/c4ay01775g>.
- [54] H. Dridi, L. Haji, A. Moadhen, Rough SERS substrate based on gold coated porous silicon layer prepared on the silicon backside surface, *Superlattice. Micro* 104 (2017) 266–270, <https://doi.org/10.1016/j.spmi.2017.02.002>.
- [55] Y. Chen, Y. Zhang, Q. Kou, Y. Liu, D. Han, D. Wang, et al., Enhanced catalytic reduction of 4-nitrophenol driven by Fe₃O₄-Au magnetic nanocomposite interface engineering: from facile preparation to recyclable application, *Nanomaterials* 8 (2018) 353, <https://doi.org/10.3390/nano8050353>.
- [56] D. Han, B. Li, Y. Chen, T. Wu, Y. Kou, X. Xue, et al., Facile synthesis of Fe₃O₄@Au core-shell nanocomposite as a recyclable magnetic surface enhanced Raman scattering substrate for thiram detection, *Nanotechnology* 30 (2019), 465703, <https://doi.org/10.1088/1361-6528/ab3a84>.
- [57] G. Premaratne, A.C. Dharmaratne, Z.H. Al Mubarak, F. Mohammadparast, M. Andiappan, S. Krishnan, Multiplexed surface plasmon imaging of serum biomolecules: Fe₃O₄@Au Core/shell nanoparticles with plasmonic simulation insights, *Sens. Actuators B-Chem.* 299 (2019), 126956, <https://doi.org/10.1016/j.snb.2019.126956>.
- [58] Y. Esmaeili, A. Zarrabi, S.Z. Mirahmadi-Zare, E. Bidram, Hierarchical multifunctional graphene oxide cancer nanotheranostics agent for synchronous switchable fluorescence imaging and chemical therapy, *Microchim. Acta* 187 (2020) 553, <https://doi.org/10.1007/s00604-020-04490-6>.
- [59] J. Gan, X. Wei, Y. Li, J. Wu, K. Qian, B. Liu, Designer SiO₂@Au nanoshells towards sensitive and selective detection of small molecules in laser desorption/ionization mass spectrometry, *Nanomedicine* 11 (2015) 1715–1723, <https://doi.org/10.1016/j.nano.2015.06.010>.
- [60] H. Elmizadeh, F. Faridbod, M. Soleimani, R.G. Ganjali, G.R. Bardajee, Fluorescent apta-nanobiosensors for fast and sensitive detection of digoxin in biological fluids using rQDs: Comparison of two approaches for immobilization of aptamer, *Sens. Actuators B-Chem.* 302 (2020) 12713, <https://doi.org/10.1016/j.snb.2019.127133>.
- [61] N. Deng, B. Jiang, Y.C. Liang, L. Zhang, Y. Liang, K. Yang, Y. Zhang, Aptamer-conjugated gold functionalized graphene oxide nanocomposites for human a-thrombin specific recognition, *J. Chromatogr. A* 1427 (2016) 16–21, <https://doi.org/10.1016/j.chroma.2015.12.018>.
- [62] C. Wang, B. Gu, Q. Liu, Y. Pang, R. Xiao, S. Wang, Combined use of vancomycin-modified Ag-coated magnetic nanoparticles and secondary enhanced nanoparticles for rapid surface-enhanced Raman scattering detection of bacteria, *Int. J. Nanomed.* 13 (2018) 1159–1178, <https://doi.org/10.2147/ijn.s150336>.
- [63] Y.K. Li, W.T. Li, X. Liu, T. Yang, M.L. Chen, J.H. Wang, Functionalized magnetic composites based on the aptamer serve as novel bio-adsorbent for the separation and preconcentration of trace lead, *Talanta* 203 (2019) 210–219, <https://doi.org/10.1016/j.talanta.2019.05.075>.
- [64] C.C. Lin, Y.M. Yang, P.H. Liao, D.W. Chen, H.P. Lin, H.C. Chang, A filter-like AuNPs@MS SERS substrate for *Staphylococcus aureus* detection, *Biosens. Bioelectron.* 53 (2014) 519–527, <https://doi.org/10.1016/j.bios.2013.10.017>.
- [65] H.J. Chang, Y.M. Yang, C.C. Lin, Y.C. Luo, H.C. Chang, H.P. Lin, et al., Using gelatin as protecting agent and organic template to synthesize noble metal nanoparticles and metal nanoparticles@mesoporous silica for SERS and CO oxidation applications, *Sens. Mater.* 20 (2009) 389–396, <https://doi.org/10.18494/SAM.2009.564>.
- [66] K. Kneipp, A.S. Haka, H. Kneipp, K. Badizadegan, N. Yoshizawa, C. Boone, K. S. Peltier, J. Motz, R. Dasari, M. Feld, Surface-enhanced Raman spectroscopy in single living cells using gold nanoparticles, *Appl. Spectrosc.* 56 (2002) 150–154.
- [67] H. Wang, Y. Zhou, X. Jiang, B. Sun, Y. Zhu, H. Wang, Y. Su, Y. He, Simultaneous capture, detection, and inactivation of bacteria as enabled by a surface-enhanced Raman scattering multifunctional chip, *Angew. Chem. Int. Ed.* 127 (2015) 5221–5225, <https://doi.org/10.1002/anie.201412294>.
- [68] K. Yuan, Q. Mei, X. Guo, Y. Xu, D. Yang, B.J. Sánchez, B. Sheng, C. Liu, Z. Hu, G. Yu, H. Ma, H. Gao, C. Haisch, R. Niessner, Z. Jiang, H. Zhou, Antimicrobial peptide based magnetic recognition elements and Au@Ag-GO SERS tags with stable internal standards: a three in one biosensor for isolation, discrimination and killing of multiple bacteria in whole blood, *Chem. Sci.* 9 (2018) 8781–8795, <https://doi.org/10.1039/c8sc04637a>.
- [69] X. Wang, Y. Huang, S. Wu, N. Duan, B. Xu, Z. Wang, Simultaneous detection of *Staphylococcus aureus* and *Salmonella typhimurium* using multicolor time-resolved fluorescence nanoparticles as labels, *Int. J. Food Microbiol.* 237 (2016) 172–179, <https://doi.org/10.1016/j.ijfoodmicro.2016.08.028>.
- [70] Y. Zhang, J. Ma, D. Wang, C. Xu, S. Sheng, J. Cheng, C. Bao, Y. Li, H. Tian, Fe-TCPP@CS nanoparticles as photodynamic and photothermal agents for efficient antimicrobial therapy, *Biomater. Sci.* 8 (2020) 6526–6532, <https://doi.org/10.1039/D0BM01427C>.
- [71] T. Shakerian Ardakani, A. Meidanchi, A. Shokri, A. Shakeri-Zadeh, Fe₃O₄@Au/reduced graphene oxide nanostructures: combinational effects of radiotherapy and photothermal therapy on oral squamous carcinoma KB cell line, *Ceram. Int.* 46 (2020) 28676–28685, <https://doi.org/10.1016/j.ceramint.2020.08.027>.
- [72] G. Baffou, I. Bordinacchini, A. Baldi, R. Quident, Simple experimental procedures to distinguish photothermal from hot-carrier processes in plasmonics, *Light Sci. Appl.* 9 (2020) 108, <https://doi.org/10.1038/s41377-020-00345-0>.

- [73] H. Wang, W. Ouyang, X. Zhang, J. Xue, X. Lou, R. Fan, Xiaonai Zhao, L. Shan, T. Jiang, Bacteria-induced aggregation of bioorthogonal gold nanoparticles for SERS imaging and enhanced photothermal ablation of gram-positive bacteria, *J. Mater. Chem. B* 7 (2019) 4630–4637, <https://doi.org/10.1039/C9TB00845D>.
- [74] J. Li, X. Liu, L. Tan, Z. Cui, X. Yang, Y. Liang, Z. Li, S. Zhu, Y. Zheng, K.W.K. Yeung, X. Wang, S. Wu, Zinc-doped Prussian blue enhances photothermal clearance of *Staphylococcus aureus* and promotes tissue repair in infected wounds, *Nat. Commun.* 10 (2019) 4490, <https://doi.org/10.1038/s41467-019-12429-6>.
- [75] H. Wang, S. Zhou, L. Guo, Y. Wang, L. Feng, Intelligent hybrid hydrogels for rapid in situ detection and photothermal therapy of bacterial infection, *ACS Appl. Mater. Interfaces* 12 (2020) 39685–39694, <https://doi.org/10.1021/acsami.0c12355>.
- [76] Y. Fu, L. Wang, X. Chi, F.A. Cesar, N. An, Y. Song, Y. Wu, P. Zhang, C. Guo, Body-clearable chromium nitride for synergetic photothermal and photodynamic treatment, *N. J. Chem.* 44 (2020) 20039–20046, <https://doi.org/10.1039/D0NJ03943H>.
- [77] Z. Wang, J. Zhang, H. Wang, J. Hai, B. Wang, Se atom-induced synthesis of concave spherical Fe₃O₄@Cu₂O nanocrystals for highly efficient MRI–SERS imaging-guided NIR photothermal therapy, *Part. Part. Syst. Charact.* 35 (2018), 1800197, <https://doi.org/10.1002/ppsc.201800197>.
- [78] F. Gao, M. Sun, L. Xu, L. Liu, H. Kuang, C. Xu, Biocompatible cup-shaped nanocrystal with ultrahigh photothermal efficiency as tumor therapeutic agent, *Adv. Funct. Mater.* 27 (2017), 1700605, <https://doi.org/10.1002/adfm.201700605>.
- [79] M. Chang, M. Wang, M. Shu, Y. Zhao, B. Ding, S. Huang, Z. Hou, G. Han, J. Lin, Enhanced photoconversion performance of NdVO₄/Au nanocrystals for photothermal/photoacoustic imaging guided and near infrared light-triggered anticancer phototherapy, *Acta Biomater.* 99 (2019) 295–306, <https://doi.org/10.1016/j.actbio.2019.08.026>.
- [80] L. Yang, B. Hu, A.H. Liu, Y. Zhang, A hollow-structured nanohybrid: intelligent and visible drug delivery and photothermal therapy for cancer, *Talanta* 215 (2020), 120893, <https://doi.org/10.1016/j.talanta.2020.120893>.
- [81] Y. Hao, B. Zhang, C. Zheng, R. Ji, X. Ren, F. Guo, et al., The tumor-targeting core-shell structured DTX-loaded PLGA@Au nanoparticles for chemo-photothermal therapy and X-ray imaging, *J. Control. Release* 220 (2015) 545–555, <https://doi.org/10.1016/j.jconrel.2015.11.016>.
- [82] H. Ke, J. Wang, S. Tong, Y. Jin, S. Wang, E. Qu, et al., Gold nanoshelled liquid perfluorocarbon magnetic nanocapsules: a nanotheranostic platform for bimodal ultrasound/magnetic resonance imaging guided photothermal tumor ablation, *Theranostics* 4 (2014) 12–23, <https://doi.org/10.7150/thno.7275>.
- [83] C. Chen, S. Wang, L. Li, P. Wang, C. Chen, Z. Sun, et al., Bacterial magnetic nanoparticles for photothermal therapy of cancer under the guidance of MRI,

Biomaterials 104 (2016) 352–360, <https://doi.org/10.1016/j.biomaterials.2016.07.030>.

Wenshi Zhao received her bachelor's degree from Jilin Normal University in 2018, and she is currently a PhD student in Changchun Institute of Optics, Fine Mechanics and Physics, Chinese Academy of Sciences, University of Chinese Academy of Sciences. She is interested in aptamer functionalized nanomaterials for SERS biosensors applications and the development of biological detection technology.

Daxin Zhang is currently a PhD student at Changchun Institute of Optics, Fine Mechanics and Physics, Chinese Academy of Sciences, University of Chinese Academy of Sciences. Her main research focuses on the applications of SERS in the field of fuel cells.

Tianxiang Zhou is a master graduate student at Jilin Normal University. Her research interests include preparation and application of SERS-based nanostructure.

Jie Huang is a master graduate student at Jilin Normal University. His research works focus on synthesis of nanomaterials.

Yushan Wang is a college student at Jilin Normal University.

Boxun Li is currently a PhD student at Jilin University. His current research interest is organic synthesis of chiral functional materials.

Lei Chen received his doctoral degree under Prof. Bing Zhao's supervision from Jilin University in 2011. Currently, he works as an associate professor at Jilin Normal University, and his research is focused on the fabrication of SERS-active nanostructure, and development of SERS-based novel sensing methods in biological field.

Jinghai Yang is a professor of Jilin Normal University. He is mainly engaged in the research of semiconductor optoelectronic materials and devices, surface-enhanced Raman, high-voltage optoelectronic materials, multiferroic materials and solid oxide fuel cells.

Yang Liu is a professor of Jilin Normal University and his research interests include the design and development of magnetic multifunctional nanocomposite materials and their application in specific SERS detection and catalytic degradation of organic pollutants in the environment.